Comparison of Porosity Distribution within Selected North American Shale Units by SEM Examination of Argon-ion-milled Samples

Chapter *in* AAPG Memoir · October 2013

DOI: 10.1306/13391710M1023588

CITATIONS
8

READS
302

5 authors, including:

James M. Rine
Wayne State University
24 PUBLICATIONS **505** CITATIONS
SEE PROFILE

Kultaransingh Hooghan
Weatherford Laboratories
23 PUBLICATIONS **465** CITATIONS
SEE PROFILE

12

James M. Rine, Erin Smart, William Dorsey, Kultaransingh Hooghan, Michael Dixon, 2013, Comparison of porosity distribution within selected North American shale units by SEM examination of Argon-ion-milled samples, *in* W. Camp, E. Diaz, and B. Wawak, eds., Electron microscopy of shale hydrocarbon reservoirs: AAPG Memoir 102, p. 137–152.

Comparison of Porosity Distribution within Selected North American Shale Units by SEM Examination of Argon-ion-milled Samples

James M. Rine, Erin Smart, William Dorsey, Kultaransingh Hooghan, and Michael Dixon

Weatherford Laboratories, 5200 N. Sam Houston Parkway West, Suite 500, Houston, Texas, 77086, U.S.A. (e-mails: james.rine@weatherfordlabs.com, erin.smart@weatherfordlabs.com, will.dorsey@weatherfordlabs.com, bobby.hooghan@weatherfordlabs.com, mike.dixon@weatherfordlabs.com)

ABSTRACT

The distribution of nanometer-size pores in ten selected Eagle Ford Group, Haynesville, Marcellus, and Barnett shale samples was similar when comparing relative numerical abundances of maximum pore diameters but not when comparing relative abundances of pore areas (pore sizes). Differences also existed between units in the association of pores with organic material. Pores were measured on argon-ion-milled (AIM) samples and examined with a field emission environmental scanning electron microscope (SEM). One Haynesville sample was also evaluated using a focused ion beam (FIB) SEM to compare to the AIM results. With the AIM samples, pore types were subdivided into three categories—organic pores, mixed matrix/organic pores, and matrix pores—based on the amount and type of material (organic or inorganic) surrounding the pores. Organic pores are pores generally associated with kerogen macerals, whereas mixed matrix/organic pores are pores that are probably associated with bitumen or pyrobitumen. Matrix pores are not associated with any organic matter. Within the sample set studied, only the Barnett samples contained pores almost exclusively within organic particles. The majority of the maximum pore diameters were less than 100 nm within all the samples examined. Only the Barnett samples, however, had a majority of their pore areas (or porosity) comprised of pores less than 10,000 nm^2 (which is the area of an equidimensional pore with the maximum pore diameter of 100 nm).

INTRODUCTON

Electron microscopic examination of pores within mudrocks (shales and mudstones) has become much more sophisticated over the last few years, driven not only by the intense economic interests in shale gas and oil but also by the technological improvements that allow characterization of nanometer-scale features. Since 2007, electron microscopy techniques have evolved sufficiently to allow researchers to

DOI: 10.1306/13391710M1023588

identify and quantify nanometer-scale pores. Previous studies characterized mudstone porosity by documenting the frequency distribution of pore sizes. This was done by comparing maximum pore diameters (Reed and Loucks, 2007; Loucks et al., 2009) and by analyzing pore volumes (Sondergeld et al., 2010). The objective of this chapter is to demonstrate other approaches to analyzing porosity by categorizing different pore type distributions and by measuring relative abundances of pore area and volume in four mudrock units: the Mississippian Barnett, the Upper Jurassic Haynesville, the Middle Devonian Marcellus formations, and the Upper Cretaceous Eagle Ford Group. Although we believe the data sets presented in this chapter are insufficient to make broad conclusions concerning the pore systems in these rock units, it is hoped that the approaches demonstrated here will assist successive researchers with more comprehensive data sets.

This chapter compares pore type character and pore size distribution between the shales based on the results of two-dimensional (2-D) field emission environmental scanning electron microscopic (FE-ESEM) examinations of ten argon-ion-milled (AIM) processed samples (Table 1). This chapter also compares results of FE-SEM examination of one AIM Haynesville sample to the three-dimensional (3-D) focused ion beam (FIB) SEM examination of the same sample.

PREVIOUS STUDIES

Groundbreaking work at the Texas Bureau of Economic Geology in the use of argon-ion-beam milling (Reed and Loucks, 2007; Loucks et al., 2009) led to the positive identification and quantification of nanometer-scale pores observed in SEM images. Prior to this work, the amount of microporosity could be measured by core analysis, but the distribution and types of pores could only be inferred by thin-section petrography (generally with spiked resins responsive to epifluorescence) or by examination of broken sample surfaces using a standard SEM. Based on our observations of Barnett and Haynesville thin sections, however, epifluorescence is commonly not observed even in samples with significant measured porosities (5 to 10%). This is probably caused by the limited ability of the spiked resins to fully penetrate these low-permeability samples. Furthermore, SEM examination of broken mudrock sample surfaces generally cannot differentiate true pores from sampling-artifact holes caused by plucking.

The Loucks et al. (2009; p. 851) study identified nanometer-scale pores and quantified pore size distribution by first using computer software (JMicrovision) to "outline and measure all individual pores." Pore diameters were then point counted from secondary electron (SE) SEM images. Rine et al. (2010), using SE FE-SEM images, hand-digitized each pore outline and colored each pore area, which in turn were analyzed using the software ImageJ (Abramoff et al., 2004) to provide pore dimensions and pore areas. Rine et al. (2010) used SE and backscattered electron (BSE) images for pore type classifications (i.e., organic vs. matrix pores). Image analysis software, such as Avizo Fire 6.3, is used to determine porosity and pore types from 3-D data sets obtained with FIB-SEM (Ambrose et al., 2010; Sondergeld et al., 2010).

METHODOLOGY

This comparison study examined four samples from two wells in the Barnett Shale (Fort Worth Basin of central Texas), four samples from two wells in the Haynesville Formation (in the East Texas Basin), two samples from one well in the Marcellus (Appalachian Basin), and two samples from one well in the Eagle Ford Group (Maverick Basin) (Figure 1; Table 1). Samples were selected based on range of total organic carbon (TOC), crushed rock (matrix) porosity values (Luffel and Guidry, 1992), and sample availability.

Sample Preparation and Microscopy

Samples were mounted on stubs and hand-polished (using 600- or 1000-grit sandpaper) prior to argon-ion milling with a Jeol SM-09910 mill. Fluids were not removed from the samples prior to processing. The advantage of argon-ion milling over mechanical polishing is that it can create a polished surface with minimal artifacts, such as surface abrasion marks and grinding debris (Loucks et al., 2009). After a light coating with gold, samples were examined with an FEI Quanta FEG-650 field emission environmental SEM (FE-ESEM) at magnifications ranging from $\times$500 to $\times$200,000 to determine the range of pore sizes present in each mudrock unit. Although representative areas of the milled surfaces (approximately 1 mm^2) in each sample were targeted for examination, undoubtedly some sample bias exists toward areas of higher pore density in order to acquire a sufficient number of pores to compare. The FE-ESEM is used to obtain high-resolution BSE and SE electron images 2-D of the milled surface. The BSE images show compositional variations, and the SE images highlight topography, such as depressions

Figure 1. Map depicts general boundaries of basins where samples from this survey originated. Table 1 lists samples used for this study, including counties where wells are located.

Table 1

Formation	County, State	Sample ID	Sample Depth Top (ft)	Sample Depth Btm (ft)	Crushed-Rock Porosity (He)	LTOC (wt %)
Barnett	Wise County, TX	B1	7131.00	7131.10	6.4	7.76
Barnett	Wise County, TX	B2	6796.00	6796.25	1.1	1.15
Barnett	Wise County, TX	B3	6685.30	6685.65	4.2	7.39
Haynesville	Shelby County, TX	H2	12079.35	12079.60	6.1	5.46
Haynesville	Red River Parish, LA	H3	12457.10	12457.20	7.0	1.49
Haynesville	Red River Parish, LA	H4	12668.30	12668.40	8.2	2.46
Marcellus	Somerset County, PA	M1	5491.00	5491.05	3.0	0.19
Marcellus	Somerset County, PA	M2	5631.00	5631.05	4.5	3.59
Austin Chalk - Eagle Ford	DeWitt County, TX	EF1	14335.80	14336.00	10.3	1.83
Austin Chalk - Eagle Ford	DeWitt County, TX	EF2	14325.10	14325.30	9.7	4.17

caused by pores. An advantage of FE-ESEM is two-fold. First, native-state samples (including samples that are wet or oily) can be examined, generally at low vacuum. Second, high-resolution 2-D images (down to nanometer size range) can document the characteristics of very-fine-grain unconventional reservoir rock samples, generally at high vacuum. For this study, all samples were examined using high vacuum pressure (to improve image resolution) and with an electron beam energy of 15 kV.

Pore Identification (FE-ESEM)

By FE-ESEM, pores were identified with SE images based on their degree of darkness (relatively deep portions of pores are generally black) and their generally bright edges (Figure 2). The edges of the pores are brighter because of the higher SE signal along the juncture of the inside surface of the pore and outer milled surface (Reimer, 1993). The pore areas bounded by these bright edges are often larger than the pore areas that are black because they include relatively shallow portions of a pore that are visible in the SE image (Figure 2). Because image-processing software available to us, such as Avizo Fire 6.3 software and Adobe Photoshop 6.0, only delineate the black (relatively deep) portions of the pores, this study hand-digitized each pore outline, then filled each pore area with a designated color.

Pore types were subdivided into three categories: organic pores, mixed matrix/organic pores, and matrix pores. Organic pores were defined based on the presence of organic material along three or more sides of the pore or greater than 75% of the diameter in the case of a circular pore. Mixed matrix/organic pores were defined as pores with one or two sides abutting organic material or less than 75% of the diameter in the case of a circular pore. The rationale for distinguishing a mixed matrix/organic pore was that these pores may be more likely associated with bitumen or pyrobitumen (secondary expelled and migrated hydrocarbons) versus an organic pore, which was more likely present within kerogen macerals deposited contemporaneous with the surrounding matrix material. A matrix pore was defined as a pore not contiguous with organic material.

The presence of organic matter was identified using BSE images because of the ability of BSE to record variations in composition (mean atomic number; Figure 3). Materials with low mean atomic number, such as carbon, exhibit low BSE intensity and are scaled as darker regions in SEM images. We consider this criterion of delineating pore types based on the relationship of the pore to organic material to be less interpretive than the pore classification schemes used by Loucks et al. (2010), which defined pores as "interparticle" or "intraparticle" and requires delineating particle boundaries.

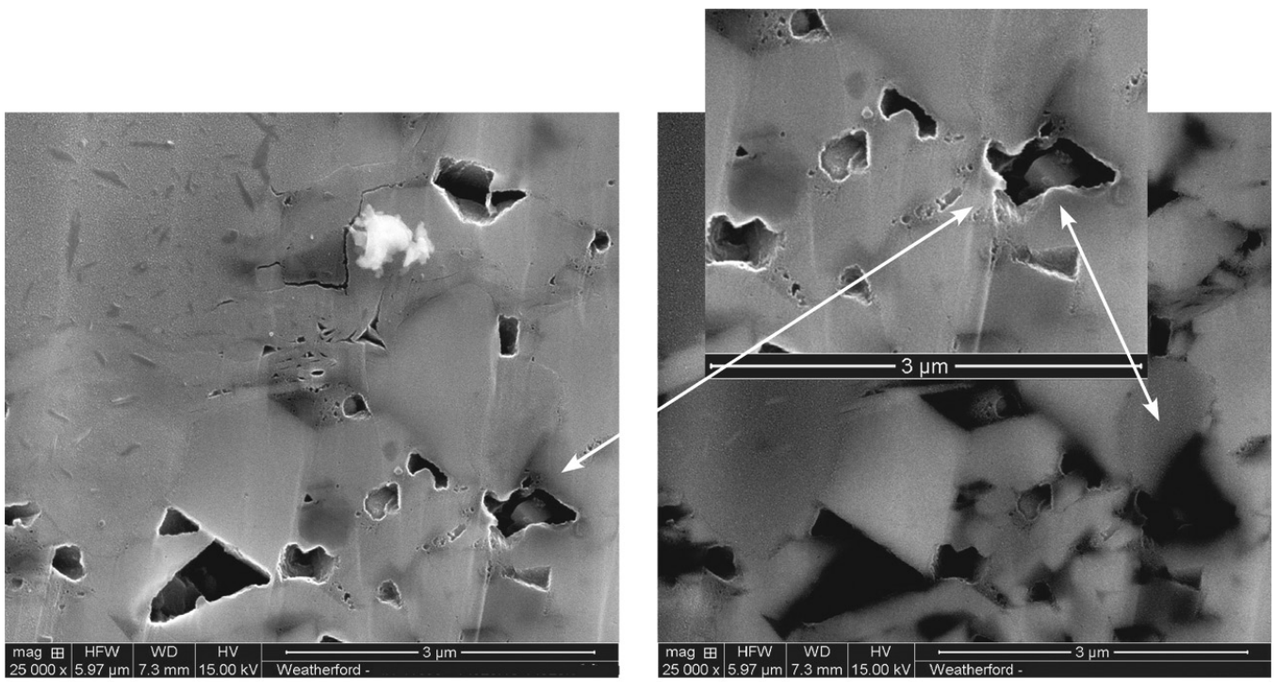

Figure 2. Pores were identified with secondary electron (SE) images based on their darkness (central portions of pores are generally black) and their generally bright edges. Note that some pore areas within the SE images bounded by bright edges are commonly larger than the black area within the pore. Also, some pores in the SE images do not include black areas. Black areas within the backscattered electron (BSE) image depict the presence of pore space or organic material.

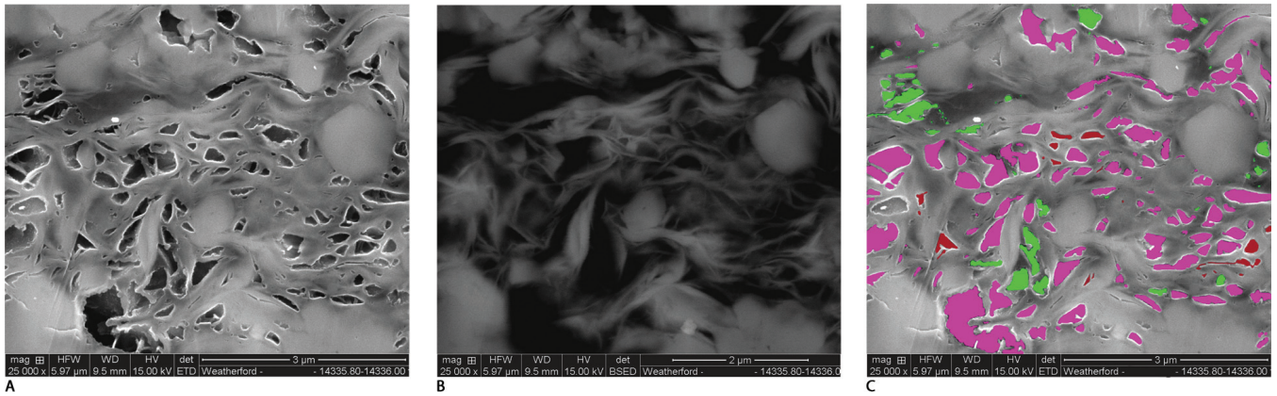

Figure 3. Images are of an Eagle Ford Group sample (EF2; Table 1). The images, which are of the same field of view, include a secondary electron (SE) image (A), a backscattered electron (BSE) image (B), and an analyzed image (C) in which pores have been colored and delineated as organic (green), mixed matrix/organic (pink), and matrix (red) pores. Pores were identified with SE images based on their degree of darkness (central portions of pores are generally black) and their generally bright edges. Black areas within the BSE image depict the presence of pore space or organic material. Note that the majority of the matrix/organic pores had rounded borders and may be pores within skeletal particles such as foraminifera tests.

"Pore digitizing" used Adobe Photoshop 6.0 software over a background SE image. Pores were outlined and areas colored on separate layers for each pore type, then saved as JPEG files against a white background. ImageJ software analyzed these separate layers to determine number of pores, pore area, and other dimensional data.

FE-ESEM Image Analysis

Pore images derived from the FE-ESEM images, were analyzed using ImageJ (IJ 1.45m), which is a public domain digital image-processing and analysis software available from the United States National Institute of Health (http://rsbweb.nih.gov/ij/index.html). This software processes individual JPEG pore type images in two steps. First, it converts them to binary images. Second, the ImageJ software analyses the binary images, providing both a summary table, which includes the number of pores and percentage pore area, and a complete size analysis of the individual pores within the image analyzed. The complete analysis of the individual pores includes maximum diameter (termed *feret* by Image J), which is the longest distance between two points on a region of interest (in this case, an individual image of a digitized pore), and minimum diameter (*minimum feret*). Also included are the areas of the binary image of each individual pore. Although pore area is 2-D, it is commonly used (such as with thin-section point-counting methods) as an estimate for porosity, which is a volume parameter. The ImageJ analyses are unitless; consequently, the scale bars were analyzed from numerous JPEG SE images to determine that the ImageJ unit for images used in this study equals 5.795 $\pm$0.02 nm. To convert ImageJ pore areas to square nanometers, area values were multiplied by the square of 5.795 nm ($x \times 33.582$ nm^2).

FIB-SEM Image Analysis

FIB-SEM analysis was done on one Haynesville Formation sample (H4). The sample was scanned for potential locations for carrying out an Auto Slice & View™ (AS&V) data collection regime (Sondergeld et al., 2010). One location was selected, and initial scanning and subsequent slicing were carried out using an FEI Company (Hillsboro, OR) Helios 650 small dual-beam (SDB) system (Auto Slice and View G3 software package). The AS&V was carried out on the location covered by the Platinum pad. Gallium-ion-beam milling was carried out using 430-pA beam current, tilted to 53°. Under normal conditions, in an SDB, milling is carried out at 52° to the imaging beam. Process optimization dictated an additional 1° tilt for milling. Imaging was carried out at 45° incidence, 3-mm working distance. Final horizontal field width was 5.30 μm. The system was set up to mill and image up to 350 slices, each slice being 10 nm (0.010 μm thick. Imaging resolution was 2048 × 1768 pixels. The individual voxel size was $x = 0.0013$ μm; $y = 0.0018$ μm; $z = 0.0100$ μm. As each individual slice was milled, the AS&V S/W took a reference image followed by a zoomed-in location selected while the run was set up. Subsequently, individual slices were aligned using the

Avizo Fire 6.3 software package. Data were then interpreted and assimilated using the various filtering and segmentation routines available in the software package.

FE-ESEM PORE TYPES AND DISTRIBUTION

Pore Types

The Barnett stands out when comparing analyzed FE-ESEM images of all the mudrock samples examined in this study by containing almost exclusively organic pores (Figure 4). Loucks et al. (2009) and Ambrose et al. (2010) also determined that porosity within the Barnett was almost exclusively within organic material. Only a fraction of 1% of the pores in the Barnett samples examined in this study were interpreted as matrix/organic pores, and none were interpreted to be strictly matrix pores (Table 2).

Pores interpreted to be combined mixed matrix/organic pores were the most abundant pore type within the Eagle Ford, Marcellus, and Haynesville samples examined in this study (Figures 3, 5, 6, respectively). In comparing the geometry of these pores, the pores of

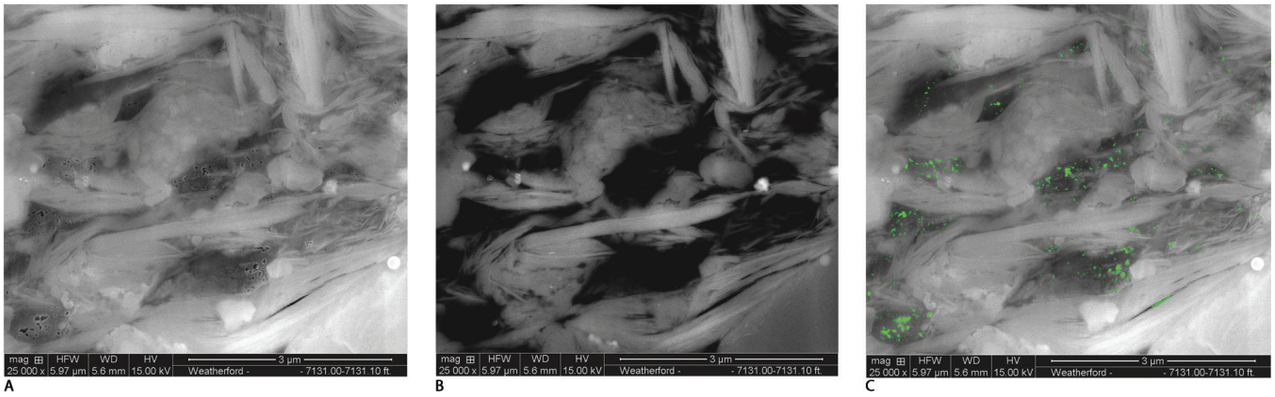

Figure 4. Images are of a Barnett sample (B1; Table 1). The images, which are of the same field of view, include a secondary electron (SE) image (A), a backscattered electron (BSE) image (B), and an analyzed image (C) in which pores have been colored and delineated as organic (green), mixed matrix/organic (pink), and matrix (red) pores. Note that no pore types other than organic pores were identified in this field of view. Pores were identified with SE images based on their degree of darkness (central portions of pores are generally black) and their generally bright edges. Black areas within the BSE image depict the presence of pore space or organic material.

Table 2

FORMATION	SAMPLES	PORE TYPE	COUNT	TOTAL AREA (ImageJ)	TOTAL AREA (nm^2)	AREA FRACTION (POROSITY %)	MAX AREA (nm^2)	MIN AREA (nm^2)	MAX DIAMETER (nm)
Barnett	SUM (B1+B2+B3)	Organic	798	32197	1.08E+06	0.75	1.07E+05	34	769
Barnett	SUM (B1+B2+B3)	Mat/Org	10	385	1.29E+04	0.02	2.46E+04	772	234
Barnett	SUM (B1+B2+B3)	Matrix	0	0	0.00E+00	0.00	0.00E+00	0	0
Barnett	SUM (B1+B2+B3)	Totals	1616	65164	2.19E+06	0.77			
Haynesville	SUM (H2+H3+H4)	Organic	527	37339	1.25E+06	1.15	6.00E+04	34	654
Haynesville	SUM (H2+H3+H4)	Mat/Org	216	82574	2.77E+06	2.77	1.40E+05	34	1166
Haynesville	SUM (H2+H3+H4)	Matrix	343	28602	9.61E+05	0.62	3.30E+04	34	481
Haynesville	SUM (H2+H3+H4)	Totals	2172	297030	9.97E+06	4.53			
Marcellus	SUM (M1+M2)	Organic	264	75973	2.55E+06	1.05	6.43E+05	34	1550
Marcellus	SUM (M1+M2)	Mat/Org	95	77526	2.60E+06	1.11	3.82E+05	34	1903
Marcellus	SUM (M1+M2)	Matrix	77	40942	1.37E+06	0.67	3.56E+05	201	1643
Marcellus	SUM (M1+M2)	Totals	436	194441	6.53E+06	2.83			
Eagle Ford	SUM (EF1+EF2)	Organic	335	84021	2.82E+06	2.21	5.36E+05	34	1282
Eagle Ford	SUM (EF1+EF2)	Mat/Org	291	324066	1.09E+07	7.58	6.85E+05	34	2553
Eagle Ford	SUM (EF1+EF2)	Matrix	178	53422	1.79E+06	1.07	2.68E+05	34	1387
Eagle Ford	SUM (EF1+EF2)	Totals	804	461509	1.55E+07	10.86			

the Eagle Ford (Figure 3) appeared to be more rounded than the matrix/organic pores of the Marcellus and Haynesville, which appeared to have more planar-edge boundaries (Figures 5, 6, respectively). The more rounded pore shapes were interpreted as pores within skeletal particles such as foraminifera tests, which are common within the Eagle Ford. The more angular pore shapes could be interpreted as being between particles or the interparticle pores of Loucks et al. (2010).

Abundance and Size Distribution

The frequency distribution of maximum pore diameters was similar for all the mudrock samples studied, with the most numerically abundant diameters less than 100 nm (Figures 7A, 8A, 9A, 10A). This frequency distribution was consistent with the results reported in the work of Loucks et al. (2009) for the Barnett Shale. The distribution was also consistent for organic pores

Figure 5. Images are of a Marcellus sample (M2; Table 1). The images, which are of the same field of view, include a secondary electron (SE) image (A), a backscattered electron (BSE) image (B), and an analyzed image (C) in which pores have been colored and delineated as organic (green), mixed matrix/organic (pink), and matrix (red) pores. Pores were identified with SE images based on their degree of darkness (central portions of pores are generally black) and their generally bright edges. Black areas within the BSE image depict the presence of pore space or organic material. Note that the majority of the matrix/organic pores have one or more straight borders and may abut inorganic particles.

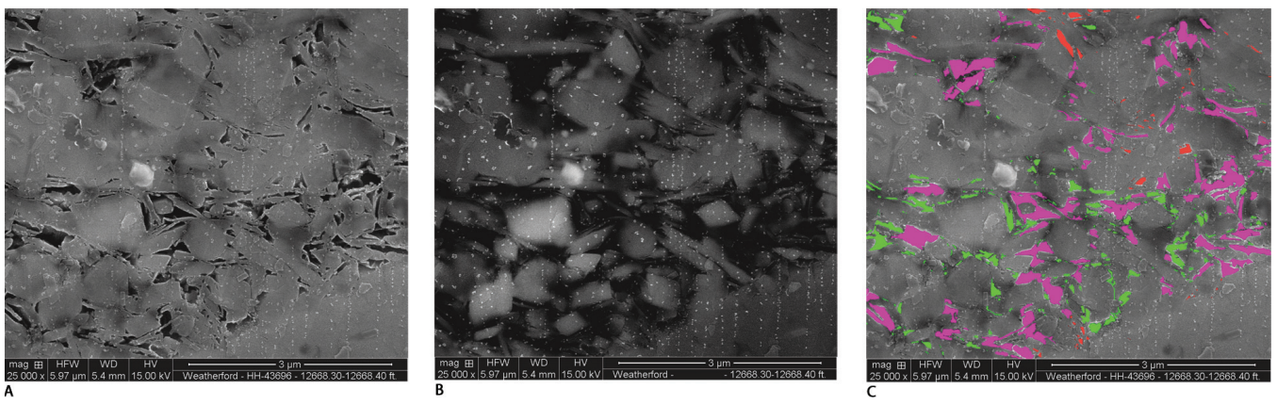

Figure 6. Images are of a Haynesville sample (H4; Table 1). The images, which are of the same field of view, include a secondary electron (SE) image (A), a backscattered electron (BSE) image (B), and an analyzed image (C) in which pores have been colored and delineated as organic (green), mixed matrix/organic (pink), and matrix (red) pores. Pores were identified with SE images based on their degree of darkness (central portions of pores are generally black) and their generally bright edges. Black areas within the BSE image depict the presence of pore space or organic material. Note that the majority of the matrix/organic pores have one or more straight borders and may abut inorganic particles.

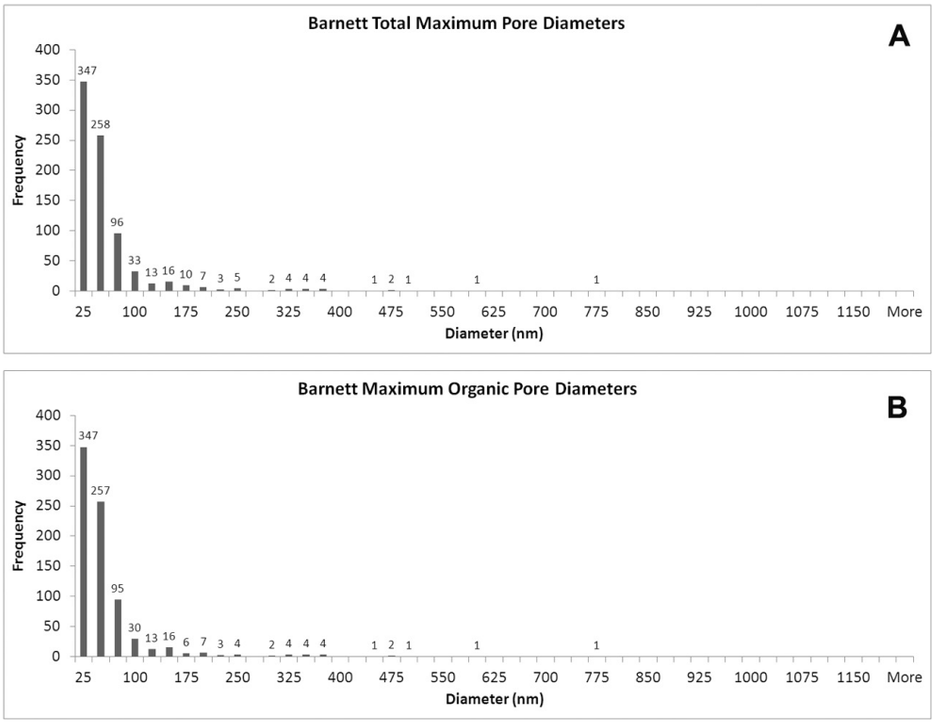

Figure 7. Histograms show the frequency distribution of pore sizes, based on maximum pore diameter, present within the Barnett samples examined in this study. The number of pores present within each diameter range is plotted at the top of each diameter range bar. (A) Total pore distribution; (B) organic pore distribution. The size distribution of matrix/organic pores present within the Barnett samples was not charted since only 10 pores of 808 total pores were so designated.

within all four units studied (Figures 7B, 8B, 9B, 10B). The size distributions for the mixed matrix/organic and matrix pores within the studied Eagle Ford, Marcellus, and Haynesville samples, however, were not as skewed to the smaller pore diameters (Figures 7C, D; 8C, D; 9C, D; 10C, D). (The Barnett samples examined only had a few matrix/organic pores, and their distribution was not charted.)

In addition to comparing pore size frequency distribution, the relative abundance of total pore areas was analyzed to understand and visualize the importance of less-numerous but larger pores. The relative abundance of pore areas was determined by subdividing the pores within size units. A total of 29 units were delineated, with the smallest pores in the 0 to 625 nm^2 (the square of 25 nm) subdivision and the largest subdivision being pore areas more than 490,000 nm^2 (the square of 700 nm). The sum of pore area within each subdivision was then divided by the total pore area of the sample to determine the percentage of the total pore area of that subdivision (Figure 11; Table 3). Within the Barnett Shale, over 55% of the porosity (pore area) resides within pores less than 10,000 nm^2 (a pore diameter of 100 nm). This pore distribution was not the same, however, within the other units. For the Haynesville samples, that fraction of the total porosity in pores smaller than 10,000 nm^2 was less than 35%. It was 7% for the Eagle Ford and 10% for the Marcellus (Table 3; Figure 11). (It should be noted that these pore area distributions may only apply to the few samples examined in this study and not to the formations generally.)

COMPARISON OF FIB-SEM AND FE-ESEM ANALYSES

Focused ion beam-SEM analysis was done on one Haynesville Shale (sample H4; Figure 12) to compare with pore distribution analysis of an FE-ESEM sample. The objective of this single comparison was to determine if the mostly computer-automated analysis of the FIB-SEM images produced similar results to the more interpretive analysis of the hand-digitized FE-ESEM images. Total porosities for the two analyses were similar (9.0% for the FIB-SEM and 10.8% for the FE-ESEM; Table 4) with differences probably caused by scale and location on the sample analyzed. These results were roughly equal to the crushed rock porosity results (8.2%; Table 1). In comparing the pore type distributions in the FIB-SEM sample with the pore type distributions of the Haynesville samples (Table 4), both results showed that "organic" pores were the least plentiful. It is important to note that the pore type definitions used for the FIB-SEM and the FE-ESEM samples were not the same. The Avizo Fire 6.3 software package interprets organic pores in

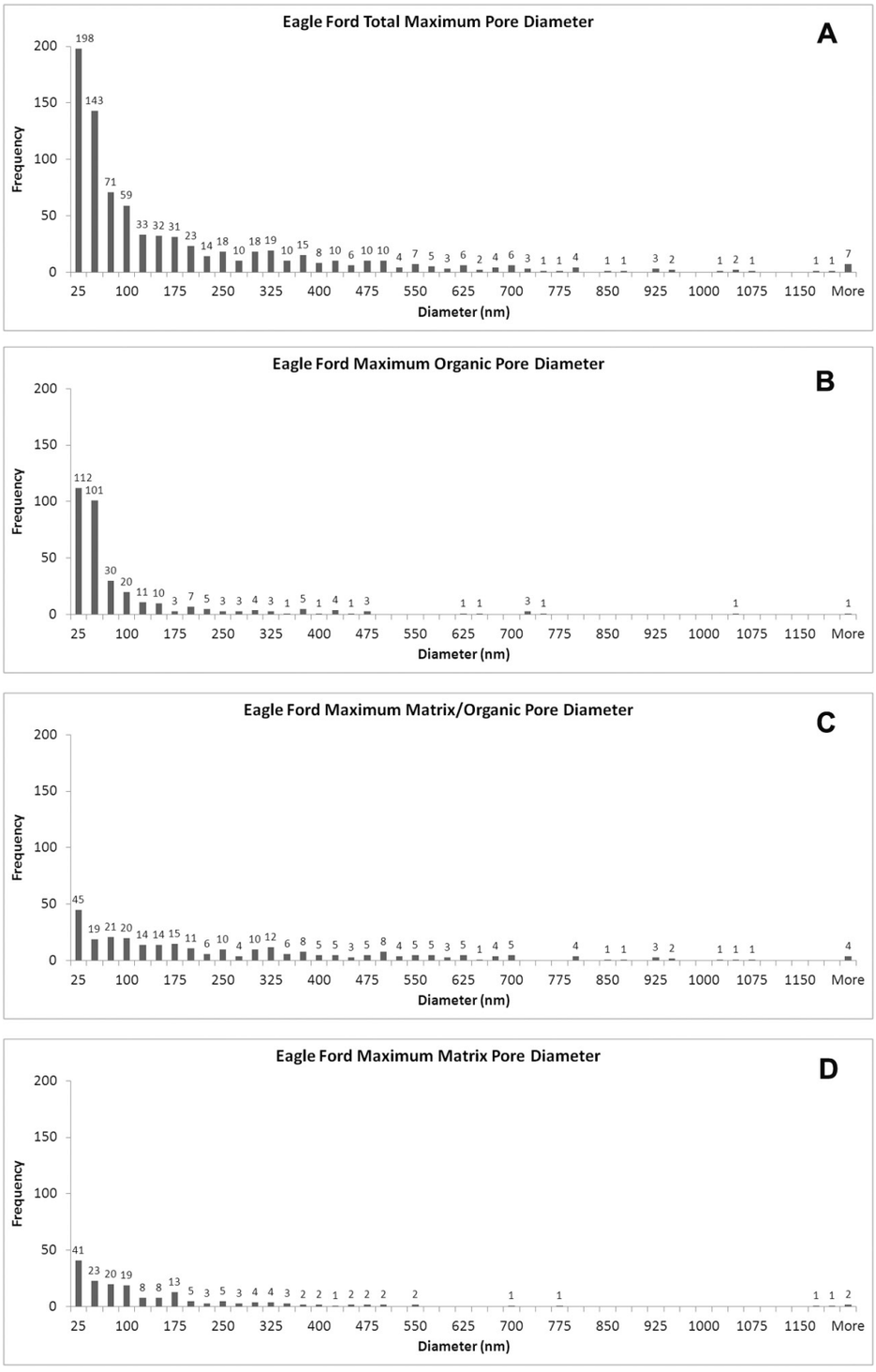

Figure 8. Histograms show the frequency distribution of pore sizes, based on maximum pore diameter, present within the Eagle Ford samples examined in this study. The number of pores present within each diameter range is plotted at the top of each diameter range bar. (A) Total pore distribution; (B) organic pore distribution; (C) matrix/organic pore distribution; (D) matrix pore distribution.

the FIB-SEM images as only those pores surrounded on six sides by organic matter, whereas the FE-ESEM analyzed samples delineated as organic pores based on the presence of organic material along three or four sides of the pore (or greater than 75% of the diameter in the case of a circular pore). Consequently, a closer comparison of the FE-ESEM results would exclude organic pores with only three sides adjoining

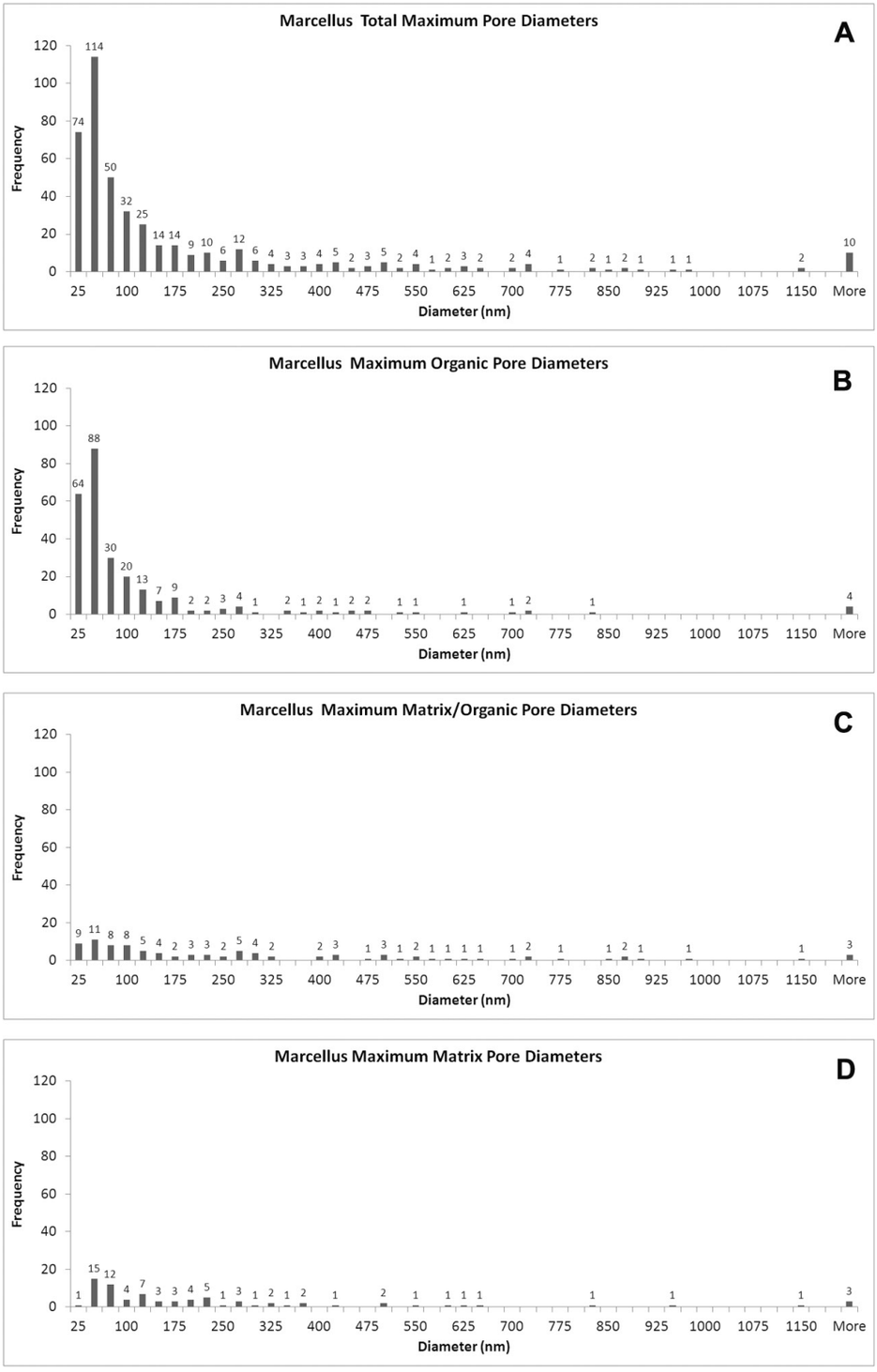

Figure 9. Histograms show the frequency distribution of pore sizes, based on maximum pore diameter, present within the Marcellus samples examined in this study. The number of pores present within each diameter range is plotted at the top of each diameter range bar. (A) Total pore distribution; (B) organic pore distribution; (C) matrix/organic pore distribution; (D) matrix pore distribution.

organics and consolidate mixed matrix/organic pores with matrix pores (FIB-SEM nonorganic porosity). Only the distribution of the total pore volumes was graphed in Figure 13 because of the different pore type designations between the FIB-SEM and FE-ESEM samples.

The frequency distribution of total pore volumes within the one Haynesville FIB-SEM sample was similar

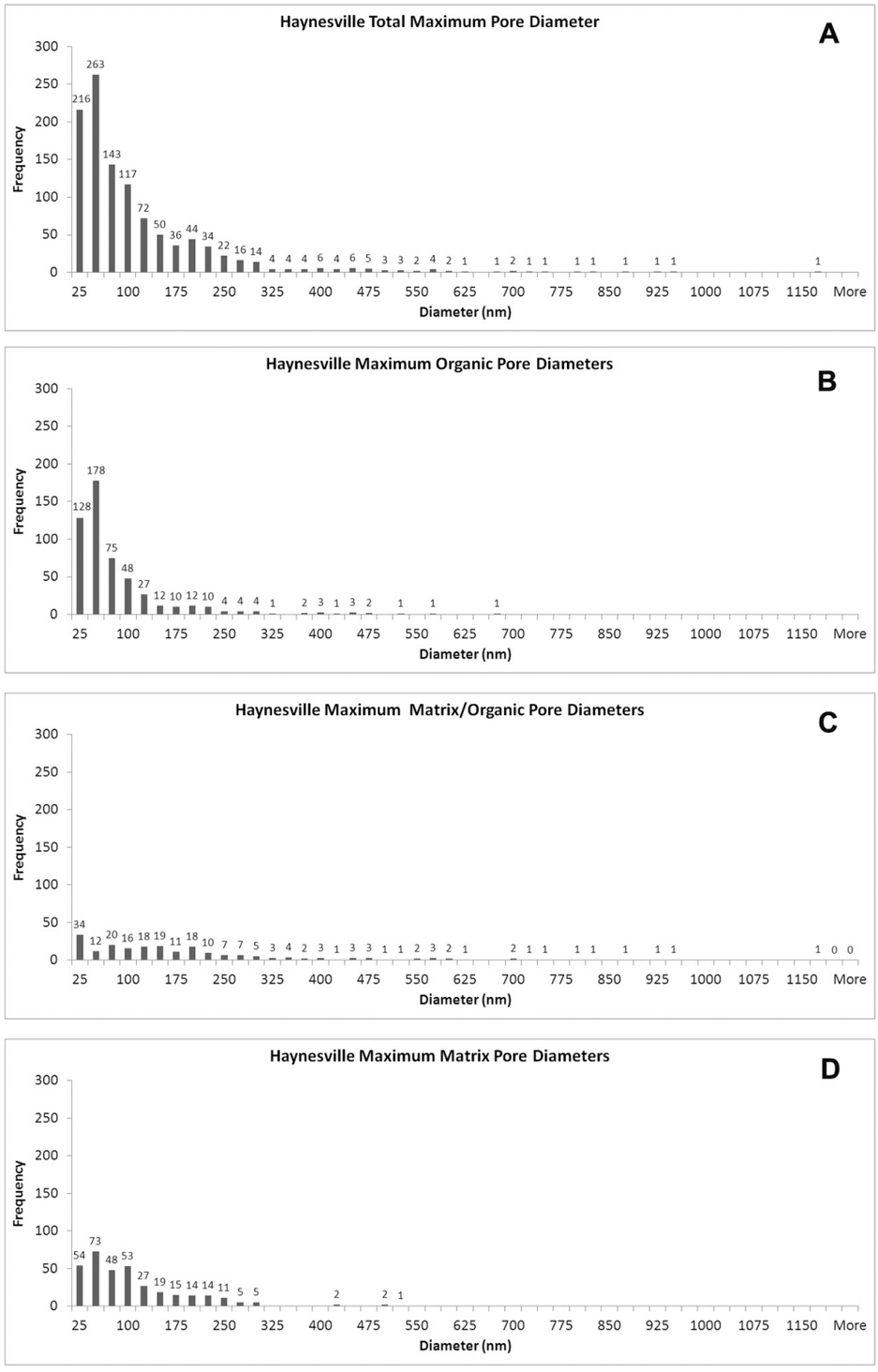

Figure 10. Histograms show the frequency distribution of pore sizes, based on maximum pore diameter, present within the Haynesville samples examined in this study. The number of pores present within each diameter range is plotted at the top of each diameter range bar. (A) Total pore distribution; (B) organic pore distribution; (C) matrix/organic pore distribution; (D) matrix pore distribution.

to the histogram of Haynesville total pore sizes based on maximum pore diameter (Figures 10A, 13A). The most numerically abundant pores had volumes equal to or less than 1.00E+06 nm^3 (the cube of 100 nm; Figure 13A).

Examination of how total porosity (pore volume) was distributed between the pore sizes present within this one Haynesville sample showed a distribution not as skewed to the smallest pores (Figure 13B). In fact,

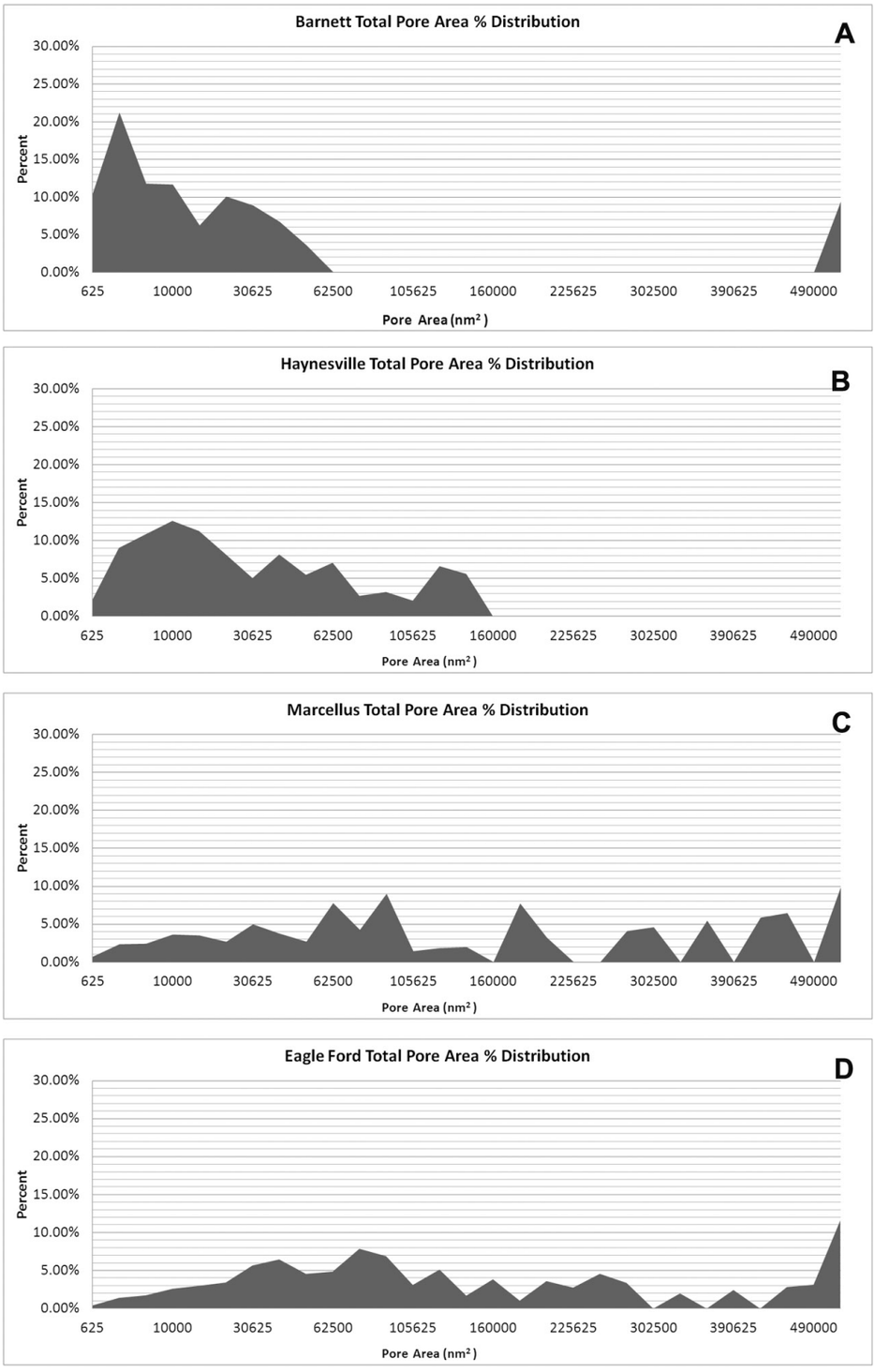

Figure 11. Charts show the differences in the relative abundance of total pore areas (two-dimensional pore sizes) between the samples from the Barnett (A), Haynesville (B), Marcellus (C), and Eagle Ford (D). The relative abundance of pore areas was determined by first subdividing the pores within size units. A total of 29 units were delineated, with the smallest pores in the 0- to 625-nm^2 (the square of 25 nm) subdivision and the largest subdivision being all pore areas more than 490,000 nm^2 (the square of 700 nm). The sum of pore area within each subdivision was then divided by the total pore area of the sample to determine the percentage of the total pore area of that subdivision. Whereas all the unit samples examined in this study had median maximum pore diameters of less than 100 nm, only the Barnett samples had a majority of their pore area (or porosity) comprised of pores less than 10,000 nm^2 (the square of 100 nm).

the larger pores appeared more volumetrically abundant in this FIB-SEM analysis than they appeared in the FE-ESEM examination (Figure 11B). The chart in Figure 13B was constructed similar to the total pore area charts in Figure 11 such that the pore volume delineations were similar, with the largest subdivision being all pore areas more than 3.43E+08 nm^3 (the cube of 700 nm) but with the smallest pore volume

Table 3

Formations	Barnett	Haynesville	Eagle Ford	Marcellus
Unit Divisions (nm^2)	Volume %	Volume %	Volume %	Volume %
625	10.5%	2.1%	0.4%	0.7%
2500	21.3%	9.0%	1.4%	2.3%
5625	11.8%	10.8%	1.7%	2.4%
10000	11.7%	12.6%	2.6%	3.6%
15625	6.2%	11.3%	3.0%	3.5%
22500	10.1%	8.2%	3.4%	2.7%
30625	8.9%	5.0%	5.7%	5.0%
40000	6.7%	8.2%	6.5%	3.7%
50625	3.6%	5.5%	4.6%	2.7%
62500	0.0%	7.1%	4.9%	7.8%
75625	0.0%	2.7%	7.9%	4.2%
90000	0.0%	3.2%	6.9%	9.0%
105625	0.0%	2.1%	3.1%	1.4%
122500	0.0%	6.6%	5.1%	1.8%
140625	0.0%	5.6%	1.7%	2.0%
160000	0.0%	0.0%	3.8%	0.0%
180625	0.0%	0.0%	1.0%	7.7%
202500	0.0%	0.0%	3.6%	3.2%
225625	0.0%	0.0%	2.8%	0.0%
250000	0.0%	0.0%	4.6%	0.0%
275625	0.0%	0.0%	3.4%	4.1%
302500	0.0%	0.0%	0.0%	4.6%
330625	0.0%	0.0%	2.0%	0.0%
360000	0.0%	0.0%	0.0%	5.5%
390625	0.0%	0.0%	2.4%	0.0%
422500	0.0%	0.0%	0.0%	5.9%
455625	0.0%	0.0%	2.8%	6.4%
490000	0.0%	0.0%	3.1%	0.0%
>490000	9.4%	0.0%	11.6%	9.8%
	100.0%	100.0%	100.0%	100.0%

subdivision being 0 to 1.56E+07 nm^3 (the cube of 250 nm). The sums of these pore areas within each subdivision are also shown in Table 5.

DISCUSSION

Although the data sets were limited, and thus likely not representative of any of the formations studied in general, it is hoped that the approaches described in this chapter will help other researchers more fully use their electron microscopy data sets. Some specific observations regarding the approaches presented in this chapter are discussed in the following.

A major benefit of electron microscopy, in addition to resolving nanometer-scale pores, is the ability to quantify the pores present using digital image analysis software. Quantification of pores with FE-ESEM samples, however, is presently labor intensive, whether the pore diameters are individually measured as with the Loucks et al. (2009) study or hand-digitized and processed with ImageJ software. The ability to delineate pore and pore types automatically from 2-D FE-ESEM images would greatly enhance the value of such examinations. Focused ion beam-SEM quantitative analyses are already automated, but the disadvantage of the FIB-SEM is that sample size is an order of magnitude smaller than the already small FE-ESEM image size. An optimum approach may be to combine the two methodologies.

Delineation of pore types with regard to their association with organic material is a critical component of electron microscopic analysis of pores within shale hydrocarbon reservoirs. With FE-ESEM samples, the presence of organic matter is based on identification of organic matter from BSE images. With FIB-SEM

Table 4

A. FIB-SEM	
FIB-SEM SAMPLE H4	**Percentage (volume %)**
Total porosity*	9.00
Porosity in organics	0.15
Nonorganic porosity	8.52
Organics	16.32
High density	0.19
Carbonate	Cannot distinguish carbonate materials from high-density materials; gray scales are too similar.

*Voxel sizes: 0.0013 × 0.0018 × 0.010 μm.

B. FE-ESEM	
FE-ESEM SAMPLE H4	**Percentage (area %)**
Total porosity	10.80
Organic pores	2.80
Mixed matrix/organic pores	8.52
Matrix pores	0.50

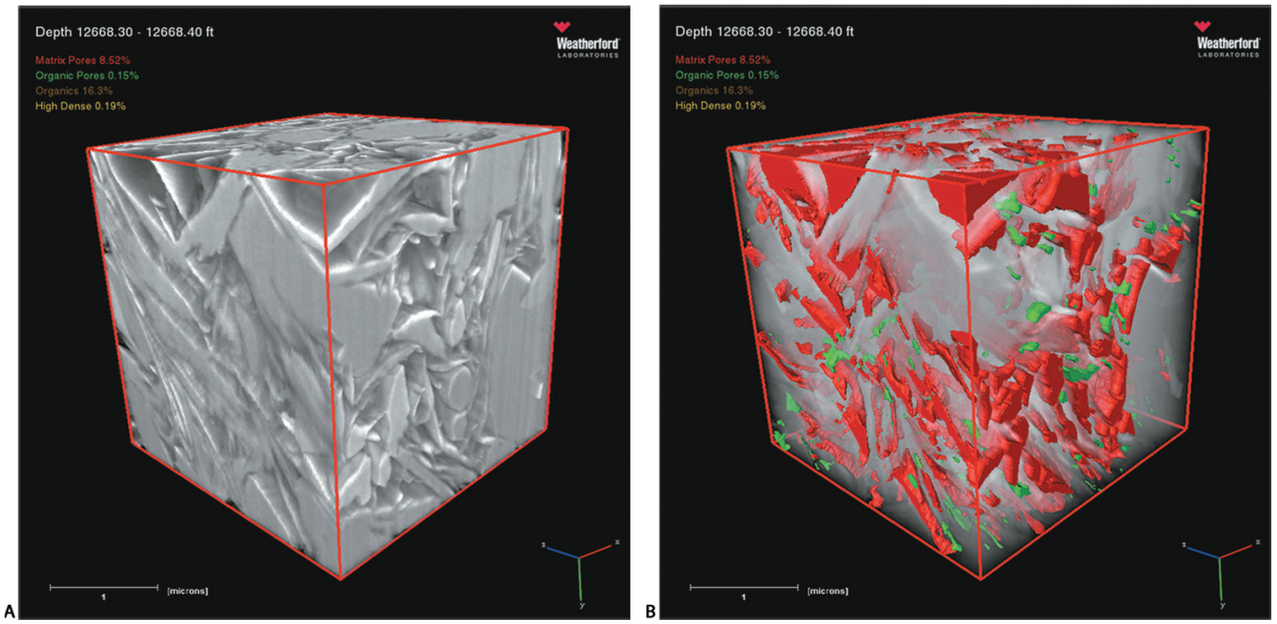

Figure 12. The three-dimensional (3-D) blocks depict one focused ion beam scanning electron microscopy (FIB-SEM) analysis done on a portion of the Haynesville sample H4. (A) Gray scale image of the FIB-SEM-analyzed sample. (B) The sample with interpreted distribution of matrix or nonorganic pores (red) and organic pores (green). The dimensions of the block were 5.30 μm wide by 3.5 μm thick. The total porosity of the FIB-SEM sample was calculated to be 9.0%, whereas the porosity by the argon-ion-milled (AIM) SEM survey was 10.8%. The crushed-rock porosity determination for this sample was 8.2% (Table 1).

examinations combined with Avizo analysis, a majority of pores interpreted as organic pores are probably within kerogen because these pores are completely surrounded by organic material. This study introduced a mixed matrix/organic pore designation to address those pores that may be associated with bitumen or pyrobitumen (secondary expelled and migrated hydrocarbons).

A better understanding of the distribution of porosity relative to pore size is important and should be considered in addition to the numerical frequency distribution of pore sizes. This is especially true for study units other than the Barnett that are not so dominated by a single pore type. Whereas the Haynesville, Marcellus, Eagle Ford, and Barnett samples examined in this study all had median maximum pore diameters

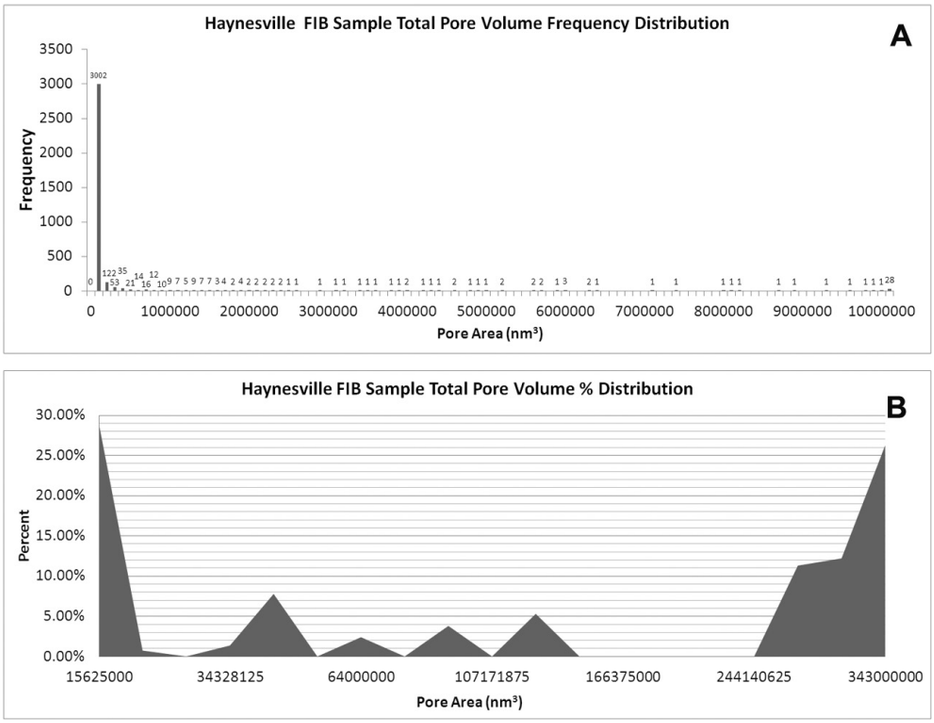

Figure 13. Frequency distribution of total pore volumes within the one Haynesville sample examined by focused ion beam scanning electron microscopy (FIB-SEM) (A) was similar to the histogram of Haynesville total pore sizes, based on maximum pore diameter (Figure 10A), with the most numerically abundant pores having volumes equal to or less than 1.00E+06 nm^3 (the cube of 100 nm). (B) Shows the distribution of total porosity (or total pore volume) between the pore sizes and reveals a distribution not as skewed to the smaller pore sizes. The chart in (B) was constructed using pore volume unit delineations that were the cubed pore diameter units in the Figure 11 charts, except the smallest unit in (B) (1.56E+07 nm^3) is the cube of 250 nm.

Table 5

Unit Divisions (nm^3)	Volume %
1.56E+07	28.93%
2.08E+07	0.73%
2.70E+07	0.00%
3.43E+07	1.36%
4.29E+07	7.77%
5.27E+07	0.00%
6.40E+07	2.39%
7.68E+07	0.00%
9.11E+07	3.79%
1.07E+08	0.00%
1.25E+08	5.30%
1.45E+08	0.00%
1.66E+08	0.00%
1.90E+08	0.00%
2.16E+08	0.00%
2.44E+08	0.00%
2.75E+08	11.29%
3.08E+08	12.19%
3.43E+08	26.25%

of less than 100 nm, only the Barnett samples had a majority of their pore area (or porosity) comprised of pores less than 10,000 nm^2 (a pore diameter of 100 nm).

CONCLUSIONS

The major conclusions derived from this study are as follows:

1. The distribution of nanometer-size pores in ten selected Eagle Ford Group, Haynesville, Marcellus, and Barnett formation samples were similar when comparing relative numerical abundances of maximum pore diameters but not when comparing relative abundances of pore areas (pore sizes). Consequently, relative distributions of pore areas should be considered when comparing mudrock units.
2. Pore types, which were subdivided into three categories (organic pores, mixed matrix/organic pores, and matrix pores), based on analysis of both SE and BSE images, showed significant distribution differences between mudrock units. Within the sample set studied, only the Barnett samples contained pores almost exclusively within organic particles.
3. For the characterization of nanometer-scale pores, SEM examination of AIM samples was a far superior methodology to thin-section petrography and standard (broken-sample) SEM examinations.

ACKNOWLEDGMENTS

We thank BP America Production Company, Samson Resources, and two anonymous companies for permitting us to examine their samples and to publish the results of those analyses. We also thank Weatherford Laboratories for the time and resources to conduct this study and, in particular, Kellen Guzman, Natalia Gonzalez, and Jeanette Kennedy for their help in processing and displaying the analytical results. Finally, we are grateful to Wayne Camp, William Demis, Keith E. Goggins, and an anonymous reviewer for their help in improving this chapter.

APPENDIX: AIM FE-ESEM IMAGE AND FIB-SEM DATA SETS

The tabular pore size data sets from the FE-ESEM and FIB-SEM examinations used in this chapter are provided as an appendix to this chapter in the CD-ROM accompanying this volume.

REFERENCES CITED

Abramoff, M. D., P. J. Magalhaes, S. J. Ram, 2004, Image processing with ImageJ: Biophotonics International, v. 11, Issue 7, pp. 36–42.

Ambrose, R. J., R. C. Hartman, M. Diaz-Campos, I. Y. Akkutlu, and C. H. Sondergeld, 2010, New pore-size considerations for shale gas in place calculations: Society of Petroleum Engineers Unconventional Gas Conference, February 23–25, Pittsburgh, Pennsylvania, SPE Paper 131772, 17 p., doi: 10.2118/131772-MS.

Loucks, R. G., R. M. Reed, S. C. Ruppel, and D. M. Jarvie, 2009, Morphology, genesis, and distribution of nanometer-scale pores in siliceous mudstones of the Mississippian Barnett Shale: Journal of Sedimentary Research, v. 79, p. 848–861.

Loucks, R. G., R. M. Reed, S. C. Ruppel, and U. Hammes, 2010, Primary classification of matrix pores in mudrocks: Gulf Coast Association of Geological Societies Transactions, v. 60, p. 435–441.

Luffel, D. L., and F. K. Guidry, 1992, New core analysis methods for measuring rock properties of Devonian Shale: Journal of Petroleum Technology, v. 4, no. 11, p. 1184–1190.

Reed, R. M., and R. G. Loucks, 2007, Imaging nanoscale pores in the Mississippian Barnett Shale of the northern Fort Worth Basin (abs.): AAPG, Annual Convention, Abstracts Volume, v. 16, 115 p.

Reimer, L., 1993, Image formation in low voltage scanning electron microscopy: Bellingham, Washington, SPIE Optical Engineering, 143 p.

Rine, J. M, W. Dorsey, M. Floyd, and P. Lasswell, 2010, A comparative SEM study of pore types and porosity distribution in high to low porosity samples from selected gas-shale formations: Gulf Coast Association of Geological Societies Transactions, v. 60, p. 825.

Sondergeld, C. H., R. J. Ambrose, C. S. Rai, and J. Moncrieff, 2010, Micro-structural studies of gas shales: Proceedings of the Society of Petroleum Engineers Unconventional Gas Conference, February 23–25, Pittsburgh, Pennsylvania, SPE Paper 131771, 17 p., doi: 10.2118/131771-MS.

U.S. National Institute of Health, ImageJ (IJ 1.45m), http://rsbweb.nih.gov/ij/index.html (accessed May 4, 2012).